

Effects of nitrogen passivation on the capture cross section energy distribution of 4H-SiC/SiO₂ interface defects and the temperature dependences of leakage current

Cite as: Appl. Phys. Lett. **127**, 122101 (2025); doi: [10.1063/5.0285027](https://doi.org/10.1063/5.0285027)

Submitted: 12 June 2025 · Accepted: 5 September 2025 ·

Published Online: 22 September 2025



View Online



Export Citation



CrossMark

Wende Huang,^{1,2} Peng Dong,^{3,a)} Nuoya Yang,¹ Yao Ma,^{1,2,a)} Qian Xu,¹ ChengWen Fu,¹ Mingmin Huang,^{1,2} Yun Li,¹ Zhimei Yang,^{1,2} Min Gong,^{1,2} Dongguo He,⁴ and Qiuming He⁴

AFFILIATIONS

¹Key Laboratory of microelectronics, College of Physics, Sichuan University, Chengdu 610065, China

²Laboratory of Radiation Physics and Technology of Ministry of Education, Sichuan University, Chengdu 610065, China

³Microsystem & Terahertz Research Center and Institute of Electronic Engineering, China Academy of Engineering Physics, Mianyang 621999, China

⁴Sichuan Xu Mao Micro Technology Co., Ltd, Suining 629200, China

^{a)}Authors to whom correspondence should be addressed: dongpeng_mtrc@caep.cn and mayao@scu.edu.cn

ABSTRACT

Nitrogen passivation has been established as an effective method to decrease the interface state density (D_{it}) for silicon carbide (SiC) devices. However, the effect of nitrogen passivation on the carrier capture cross section distributions of SiC/SiO₂ interface defects is still unclear, which is another critical factor governing the interface recombination characteristics and device performances of SiC power devices. In this work, the local band bending is regulated in deep level transient spectroscopy characterizations to modulate the carrier capture and emission behaviors of interface defects in localized energy levels. Therefore, the distribution of carrier capture cross section is determined as a function of the interface state density. Surprisingly, it is found that nitrogen passivation leads to an increase in the capture cross sections of SiC/SiO₂ interface defects, especially for deeper interface states within the bandgap. Based on those findings, the mechanisms of the temperature dependence of leakage current characteristics are explored, where the leakage currents first decrease with rising temperature, reaching a minimum at 250 K, and subsequently increase further with elevated temperature. An interfacial defect-assisted Fowler–Nordheim tunneling mechanism is proposed to explain the temperature dependence of leakage currents, which is suggested to originate from the synergistic interplay between the energy-level dependent capture cross section and interface state densities.

Published under an exclusive license by AIP Publishing. <https://doi.org/10.1063/5.0285027>

As a representative third-generation wide-bandgap semiconductor material, the 4H polytype of silicon carbide (4H-SiC) has attracted significant attention in high-power electronics due to its exceptional physical properties, including a wide bandgap (~ 3.3 eV), high critical breakdown field (~ 3 MV/cm), and excellent thermal conductivity.^{1,2} The native SiO₂ layer formed through thermal oxidation enables 4H-SiC metal–oxide–semiconductor field-effect transistors (MOSFETs) to inherit silicon-based process compatibility while achieving higher operating temperatures and power densities.^{3,4} However, the performance of 4H-SiC MOSFETs remains severely constrained by two critical challenges: low channel mobility and gate oxide reliability issues. These limitations primarily originate from the high density of traps,

which exhibit complex energy distributions across the bandgap.^{5–7} These defects can be categorized into three types: (1) interfacial defects (e.g., carbon clusters and suboxide structures) that exhibit a U-shaped density of interface state (D_{it}) distribution near the conduction band (E_C) and valence band (E_V) edges;^{8,9} (2) near-interface traps (NITs) arising from metastable Si₂-C-O configurations in the SiC/SiO₂ transition region;^{10,11} and (3) oxide defects (e.g., oxygen vacancies) whose charge trapping behavior exacerbates V_{th} instability at elevated temperatures.¹²

Multiple passivation approaches, including NO/N₂O, POCl₃,^{13–15} NH₃ plasma,¹⁶ and N₂ annealing,^{17,18} have been developed to suppress D_{it} at SiC/SiO₂ interfaces. The POCl₃-POA technique enables D_{it}

reduction at relatively low processing temperatures,¹⁹ primarily through phosphorus atom incorporation, which effectively passivates tri-coordinated carbon defects and eliminates interface states. However, its acute toxicity and adverse electrical side effects limit practical adoption. NH₃ plasma passivation demonstrably reduces D_{it} , yet inadvertently introduces additional electron traps that induce threshold voltage (V_{th}) instability in fabricated devices.^{16,20} In contrast, NO/N₂O passivation offers unique advantages for D_{it} mitigation. Its core strength lies in the direct and efficient delivery of active nitrogen species to the SiC/SiO₂ interface, preferentially passivating the most recalcitrant carbon-related defects. This mechanism achieves substantial suppression of near-conduction-band edge D_{it} , as evidenced by conductance measurements in prior studies.²¹ A significant enhancement in electron mobility has been reported following high-temperature anneals in NO, reaching up to $30\text{--}40\text{ cm}^2 \cdot \text{V}^{-1} \cdot \text{s}^{-1}$.²² Consequently, NO/N₂O annealing has emerged as the industrially preferred technique for commercial SiC power devices.

However, two critical challenges remain unresolved in nitrogen-passivated SiC devices: the persistent V_{th} drift caused by oxide charge accumulation and the unclear mechanisms governing the electrical recombination activity of interfacial defects, which affect device reliability.^{23,24} These limitations arise from the inability of conventional characterization methods (e.g., $C\text{--}V$) to decouple the contributions of interface and oxide defects, as well as the lack of quantitative analysis of carrier capture cross section. Although Lelis *et al.* elucidated the charge exchange mechanism of NITs through a dual-tunneling model, they did not clarify how nitrogen passivation modifies electrical activity.²⁵ Similarly, Fiorenza *et al.* observed anomalous temperature dependence of Fowler–Nordheim (FN) tunneling currents in nitrogen-passivated devices²⁶ but failed to correlate this phenomenon with carrier capture behavior.

This study provides a comprehensive investigation into the regulation mechanisms of nitrogen passivation on the electrical activity of SiC/SiO₂ interface, especially the dependence of carrier capture behaviors on the energy levels. By employing localized band bending modulation in the deep level transient spectroscopy (DLTS) characterizations, the distribution of carrier capture cross sections is determined as a function of energy levels arising from the nitrogen passivated SiC/SiO₂ interface defects. Based on the determined carrier capture cross section and interface state density distributions, the temperature dependence of the leakage current of SiC MOS devices is thoroughly explained through a defect-assisted Fowler–Nordheim tunneling model.

The MOS capacitor devices were fabricated at the No. 55 Research Institute of China Electronics Technology Group Corporation using the following process: commenced with n -type 4° off-axis 4H-SiC (0001) wafers, on which a 5- μm -thick epitaxial layer with a doping concentration of $1 \times 10^{16}\text{ cm}^{-3}$ was grown. A 45-nm-thick oxide layer was thermally grown via dry oxidation at 1200 °C for 40 min on the epitaxial layer to form the standard oxide samples. Subsequently, nitrogen-passivated samples were prepared by subjecting these standard oxide samples to post-oxidation annealing in NO ambient at 900 °C for 30 min. The SiO₂ thickness is approximately 45 nm, which is determined by spectroscopic ellipsometry. Then, a 150-nm-thick Ni ohmic contact was formed on the backside via thermal evaporation, while the front-side gate electrodes ($1 \times 1\text{ mm}^2$ square geometry) were patterned through sequential deposition of 1000-nm Ti and 4- μm Al layers. Electrical characterization was performed using an Agilent B1500A

semiconductor parameter analyzer across a temperature range of 100–375 K. For $C\text{--}V$ measurements, a 1 MHz small-signal AC voltage with 100 mV amplitude was applied.

DLTS measurements were conducted on both standard oxide and nitrogen-passivated samples across a temperature range of 100–650 K to investigate the effects of nitrogen passivation on defect recombination activity. The transient capacitance spectra and temperature control were obtained using a Phystech FT1030 HERA-DLTS system coupled with a Linkam HFS600E-PB4 probe station. The applied reverse (V_R) and pulse (V_P) voltages correspond to depletion and accumulation states of the MOS capacitor between gate and drain, respectively. A fixed period width (T_W) of 204.8 ms and pulse width (t_p) of 10 ms ensured the effective population of the interface trap. In small-pulse testing, V_R was incrementally adjusted from deep depletion to weak accumulation, with a 0.25 V difference maintained between V_P and V_R . The energy level ($E_C\text{--}E_T$) and D_{it} were determined from temperature-dependent DLTS signals by^{27–29}

$$E_T = E_C - kT \ln(K\sigma_n T^2 \tau_0), \quad (1)$$

$$K = 2(3)^{1/2} k m_{\text{eff}} \left(\frac{2\pi}{h^2} \right)^{3/2}, \quad (2)$$

$$D_{it} = \varepsilon_{\text{SiC}} C_{\text{acc}} A N_{\text{dop}} \Delta C / (C_R^3 k T \beta), \quad (3)$$

where E_T denotes the defect energy level, specifically defined as the energy difference relative to the conduction band edge of SiC. σ_n represents the capture cross section, τ_0 denotes the emission rate window proportional to the period width T_W , and ε_{SiC} corresponds to the dielectric constant of SiC. C_{acc} and C_R refer to the oxide capacitance in accumulation and the MOS depletion capacitance, respectively, corresponding to the capacitances under V_P and V_R . A indicates the effective capacitor area, N_{dop} is the substrate doping concentration, and ΔC is the capacitance transient amplitude, which is proportional to DLTS signal intensity. The capture cross section σ_n is extracted from the Arrhenius dependence of the time constants on temperature, with the energy-averaged σ_n applied in the D_{it} calculations. β represents the energy resolution factor (2.5) for FT-DLTS.

Previous studies have shown that the electrical activity of SiC/SiO₂ interface defects is regulated by interface state density, and the capture cross section is recognized as the critical parameter determining the capture and emission behaviors of charge carriers by individual defects.^{29,30} To obtain energy-dependent capture cross section values with higher precision and characterize their distribution relative to defect energy levels, this investigation employs band edge bending modulation principles in temperature-variable DLTS measurements.²⁹ The small-pulse DLTS methodology enables high-resolution probing of capture cross sections within localized energy ranges by controlling pulse voltage increments ($\Delta V = 0.25\text{ V}$). Quantitative extraction of capture cross sections at distinct energy levels is achieved through Arrhenius curve slope analysis and DLTS peak shift evaluation. Figures 1(a) and 1(b) present the small-pulse DLTS results, while Fig. 1(c) compares the energy-resolved capture cross section distributions between nitrogen-passivated and standard thermal oxide samples. Both sample types exhibit a sharp decrease in capture cross sections near the conduction band edge, consistent with prior reports.^{31–34} Notably, defects located deeper within the bandgap (farther from E_C) demonstrate larger capture cross sections and enhanced electrical recombination activity at elevated temperatures.

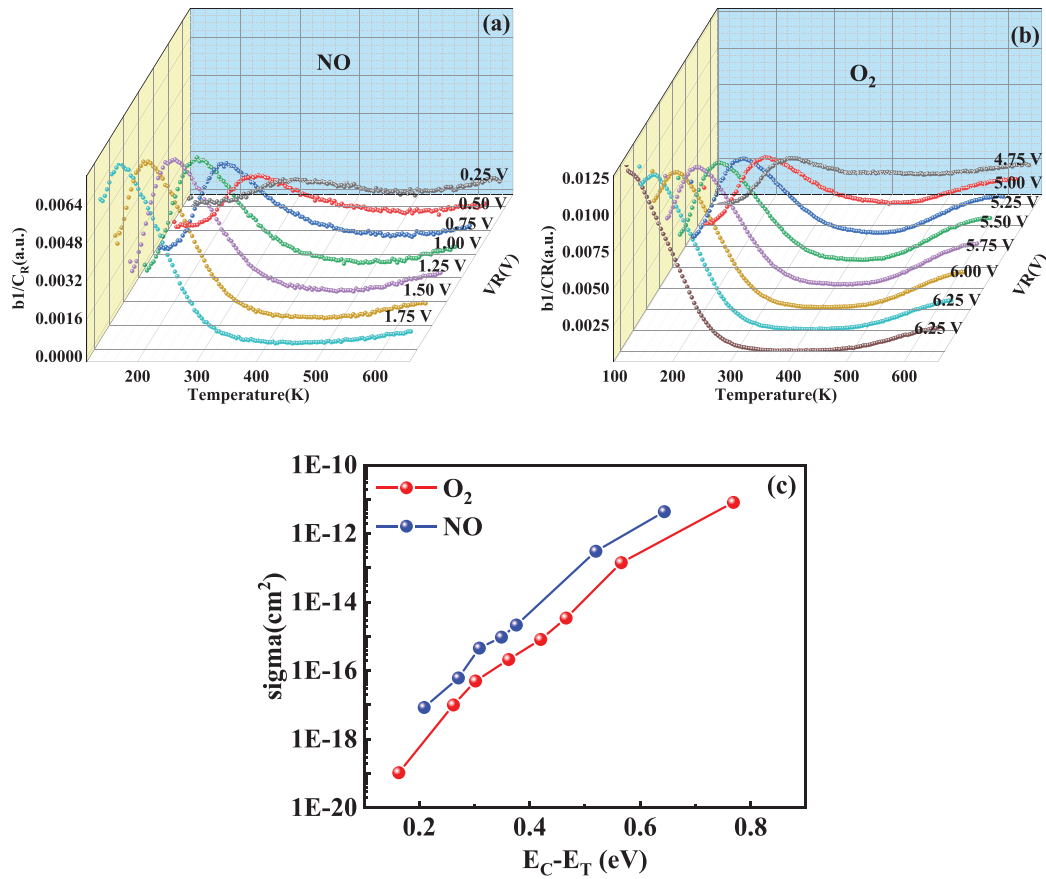


FIG. 1. (a) Small-pulse DLTS results of nitrogen-passivated samples and (b) conventional thermal oxide samples. (c) Energy-resolved defect capture cross section distribution of conventional thermal oxidation and nitrogen-passivated samples.

Interestingly, nitrogen-passivated samples exhibit a slight increase in capture cross section compared to conventional thermal oxides, which is potentially linked to nitrogen-induced interfacial reconstruction. First-principles calculations reveal that nitrogen passivation replaces interfacial carbon dimers ($C=C$) and metastable Si_2-C-O structures with stable $Si\equiv N$ bonds,³⁵ thereby eliminating shallow-level defects arising from dangling bonds.^{10,11,36} However, nitrogen doping concurrently generates deep-level defects (e.g., $N-Si-O$ complexes), whose stronger localized states result in larger capture cross sections.^{32,37} Deák *et al.* further demonstrate that nitrogen-modulated $Si-O$ bonding reduces the thickness of the interfacial suboxide layer, although partially unpassivated tri-coordinated configurations may still act as deep-level trapping centers.¹⁰

By adjusting V_R and V_P to transition the MOS capacitor from depletion to accumulation states, DLTS measurements were performed to investigate the impact of nitrogen passivation on interface state density distributions. Figure 2(a) presents the DLTS spectra for nitrogen-passivated and conventional thermally oxidized samples, where broad DLTS peaks located from 100 to 350 K are observed. This DLTS signal shows good agreement with the constant-capacitance DLTS spectra for the interface states in thermally oxidized and NO-annealed $SiO_2/4H-SiC$.³³ Based on Fig. 2(a) and Eqs. (1)–(3), the distributions of

interface state density as a function of energy level are derived and shown in Fig. 2(b). It is revealed that the interface state density decreases rapidly from near the conduction band edge (from $E_C-0.2$ eV to $E_C-0.8$ eV), with no significant variation at deeper energy levels. The D_{it} distribution aligns with acceptor-like electron traps ($C=C$ pairs and NITs), suggesting these defects as probable contributors to the observed D_{it} signals. Compared to conventional thermal oxidation samples, nitrogen passivation significantly reduces the interface state density, which is attributed to nitrogen-induced passivation of interfacial defects.

To elucidate the mechanism of nitrogen passivation on leakage current characteristics in SiC MOS devices, the $J-E$ characteristics of nitrogen-passivated and conventional thermal oxidation samples were characterized across a temperature range of 100–375 K. The leakage current density and oxide electric field were calculated using the following equations:

$$J = \frac{I_{\text{leakage}}}{A}, \quad (4)$$

$$E = \frac{V_G - V_{FB}}{t_{ox}}, \quad (5)$$

where V_G is the gate voltage applied during testing, V_{FB} is the temperature-dependent flatband voltage, t_{ox} is the oxide thickness, and A is the electrode area of the oxide layer.

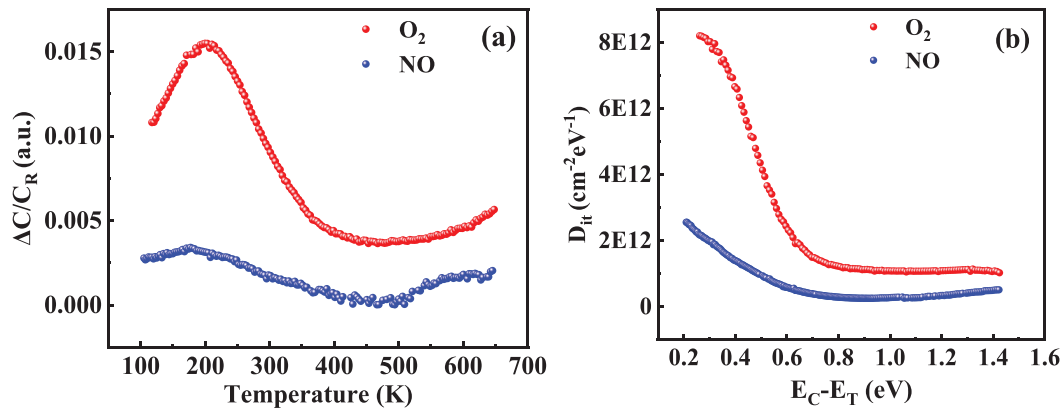


FIG. 2. (a) DLTS spectra and (b) energy-resolved interface state density distribution of conventional thermal oxidation and nitrogen-passivated samples.

The observed high leakage current does not stem from the hard breakdown of the oxide layer. Instead, it arises from FN tunneling, which becomes the dominant leakage mechanism. Herein, the electrons traverse the triangular potential barrier from the semiconductor into the metal electrode. This phenomenon is considered a “soft breakdown.”

Figure 3 presents the J - E characteristics of thermally oxidized and NO-annealed samples. It can be seen that the leakage current significantly increases with the elevated electric field. This is verified from the dominant interface defects-assisted FN tunneling, which will be discussed and shown in the next section. The leakage current onset is ~ 4 MV/cm for NO-annealed samples, while it decreases to 3–4 MV/cm for thermally oxidized samples. This discrepancy originates from abundant interfacial defects in thermally oxidized samples, which facilitates defect-assisted tunneling and therefore results in the smaller onset of electric field. In addition, the inset of Fig. 3(a) shows that the leakage current of nitrogen-passivated samples decreases with rising temperature, reaching a minimum at 250 K, and subsequently increases with further temperature elevation. The Fig. 3(b) provides a magnified view of the curve segment, where this trend is more clearly visible. In contrast, the leakage current of the conventional thermal oxidation samples monotonously decreases from 100 to 250 K, and then stabilizes with the elevated temperature [Fig. 3(c)]. Figure 3(d) illustrates the temperature-dependent current density at an electric field of 6 MV/cm, which corresponds to a typical electric field for FN tunneling in SiC/SiO₂ systems.³⁸ At this field strength, the leakage current mechanisms in both sample types are predominantly governed by FN tunneling.^{20,39} No alternative physical mechanisms contribute significantly under these conditions. The conventional thermal oxidation samples display a monotonic decrease in current density with increasing temperature, while the nitrogen-passivated samples show a distinct non-monotonic trend, likely due to competition between two current-regulating mechanisms. These anomalous temperature dependencies contradict the weak temperature sensitivity of conventional FN tunneling and the positive temperature dependence of Poole-Frenkel (PF) emission.^{40,41} More analysis integrating conduction mechanisms and the electrical activity modulation of interface defects is required to explain these observations.

To further elucidate the origin of the temperature dependence of leakage current in these samples, the conduction mechanisms were

analyzed. Previous studies have demonstrated that leakage currents in SiC/SiO₂ structures under high electric fields are typically dominated by either FN tunneling, PF emission, or a combination of both mechanisms.^{42–44} To explore the conduction mechanisms, the J - E characteristics were fitted. The current density expression for PF emission is given by⁴⁵

$$J_{\text{PF}} = (q\mu N_C)E \exp \left\{ \left[-q \left(\phi_t - \sqrt{\frac{qE}{\pi\epsilon_r\epsilon_0}} \right) \right] / kT \right\}, \quad (6)$$

$$\ln(J/E) = \frac{q}{kT} \sqrt{\frac{q}{\pi\epsilon_r\epsilon_0}} \sqrt{E} - \frac{\phi_t}{kT} + \ln(q\mu N_C), \quad (7)$$

where N_C is the conduction band density of states, μ is the electron mobility, and Φ_t denotes the defect energy level in the oxide layer (ranging between 1.1 and 1.3 eV). The fitting formula for FN tunneling is provided by⁴⁶

$$J_{\text{FN}} = AE^2 \exp(-B/E), \quad (8)$$

$$\ln(J/E^2) = \ln(A) - B/E, \quad (9)$$

$$A = \frac{q^3 m_e}{8\pi h m_{\text{ox}} \phi_B}, \quad (10)$$

$$B = \frac{4(2m_{\text{ox}})^{1/2} \phi_B^{3/2}}{3qh/2\pi}, \quad (11)$$

where m_e is the effective electron mass in the semiconductor, h is Planck's constant, m_{ox} is the effective electron mass in the oxide, and ϕ_B is the effective electronic barrier height.

It is generally accepted that the PF emission mechanism becomes prominent at temperatures above room temperature. The J - E characteristics of conventional thermal oxidation and nitrogen-passivated samples at 350 K were fitted using the PF model. Figure 4(a) shows the $\ln(J/E) - E^{1/2}$ plots for leakage currents in nitrogen-passivated and conventional thermal oxidation samples based on PF fitting. The dielectric constants (ϵ) obtained from the slopes of 2.9 and 2.8 for the nitrogen-passivated and conventional samples, respectively, were both found to be lower than the dielectric constant of SiO₂ (3.9). This suggests that PF emission is not the dominant mechanism. Figure 4(b) displays the

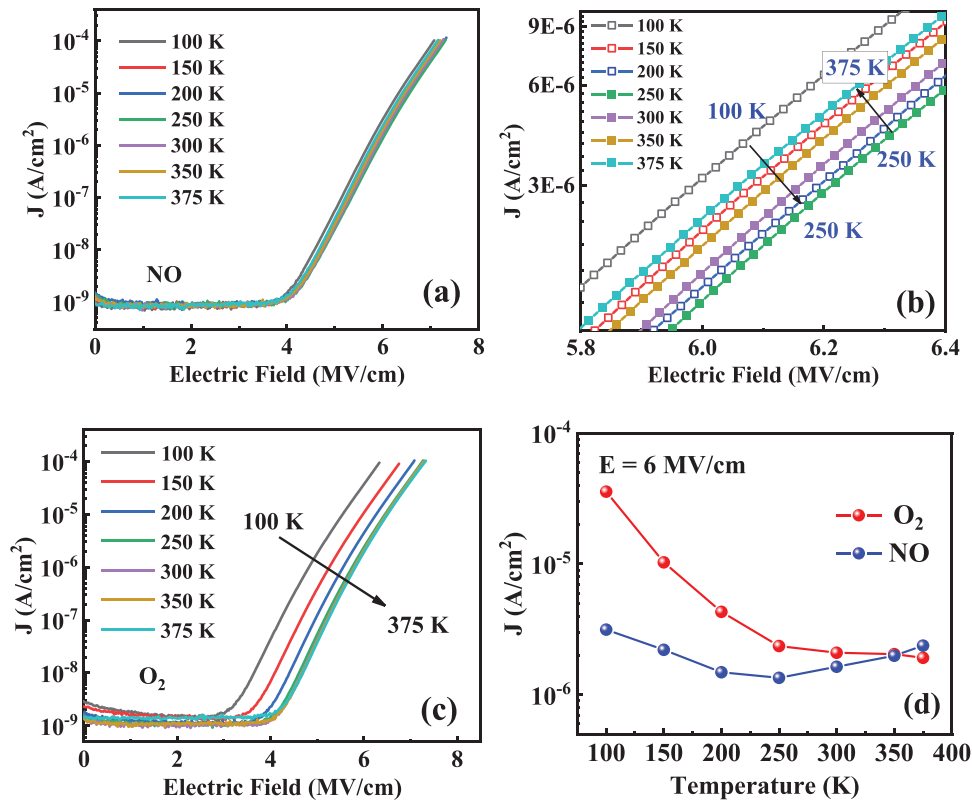


FIG. 3. (a) J - E characteristics of nitrogen-passivated samples and (c) conventional thermal oxidation samples at different temperatures. (b) The magnified view of the curve segment in Fig. 3(a), where the leakage currents at 100–200 K and 250–375 K are labeled as open and solid squares, respectively; (d) temperature-dependent current density of nitrogen-passivated and conventional thermal oxidation samples at an electric field strength of 6 MV/cm.

$\ln(J/E^2)-1/E$ curves for leakage currents based on FN fitting. Both sample types exhibit linear behavior under high electric fields at 350 K, indicating that the leakage mechanism is dominated by electron tunneling through a triangular barrier into the SiO₂ conduction band, analogous to FN tunneling. However, unlike the weak positive temperature dependence characteristic of FN tunneling, both samples exhibit a negative temperature-dependent mechanism (Fig. 3), which may be associated with defect-assisted FN tunneling.⁴⁷ The negative temperature

dependence is likely governed by temperature-dependent defect recombination dynamics.

The defect-assisted FN tunneling mechanism is illustrated in Fig. 5. The microscopic processes involved are as follows: (1) electron trapping stage (process B): electrons from the SiC conduction band (E_c) are captured by interfacial defects, forming localized charged centers; (2) interfacial defect-assisted FN tunneling stage (process C): trapped electrons tunnel into the SiO₂ conduction band via defect

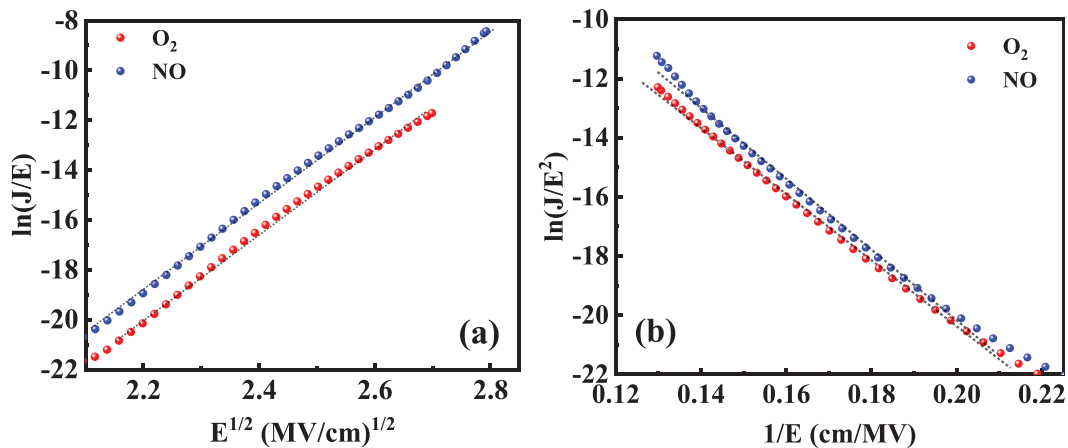


FIG. 4. (a) PF-fitted $\ln(J/E^2)-E^{1/2}$ curves and (b) PF-fitted $\ln(J/E^2)-1/E$ curves for leakage currents in conventional thermal oxidation and nitrogen-passivated samples at 350 K.

energy levels; (3) cross-interface diffusion stage (process D): a fraction of electrons further migrate to near-interfacial trap levels aligned with or energetically farther from the SiC conduction band; (4) near-interfacial defect-assisted FN tunneling stage (process E): electrons captured by near-interfacial traps (NITs) traverse the triangular barrier into the SiO₂ conduction band. This process, like process C, exhibits weak temperature dependence analogous to conventional FN tunneling.⁴⁸

The temperature-dependent regulation mechanism of leakage currents in nitrogen-passivated samples is manifested as follows: In the low-temperature regime ($T < 250$ K), the phonon-assisted escape probability of electrons trapped at interfacial/NITs is relatively low and enhances the trap occupancy,⁷ thereby enhancing defect-assisted tunneling currents. In the high-temperature regime ($T > 250$ K), thermal excitation increases the escape rate of electrons from shallow-level traps, while deep-level defects with enlarged capture cross sections dominate the tunneling process, leading to a resurgence in leakage currents [shown in Figs. 3(b) and 3(d)]. The monotonous behavior of conventional thermal oxidation samples originates from the masking effect of high interfacial and near-interfacial defect density on the electrical activity of deep-level defects. The high density of shallow-level traps at interfaces and near-interfaces in conventional samples causes rapid de-trapping at elevated temperatures, suppressing the contribution of deep-level defect-assisted tunneling and resulting in a continuous decrease in leakage currents with temperature [shown in Figs. 3(c) and 3(d)]. Stepwise DLTS measurements confirm that nitrogen-passivated samples exhibit larger defect capture cross sections but reduced D_{it} values compared to conventional samples.

This indicates that nitrogen passivation selectively eliminates shallow-level defects (e.g., Si₂-C-O structures) and induces deep-level (e.g., Si-N-O) complex defects, thereby enabling bidirectional modulation of the temperature-dependent leakage behavior. This mechanism highlights that synergistic optimization of defect energy-level distribution and capture cross sections at interfaces is critical for enhancing the high-temperature reliability of SiC MOS devices.

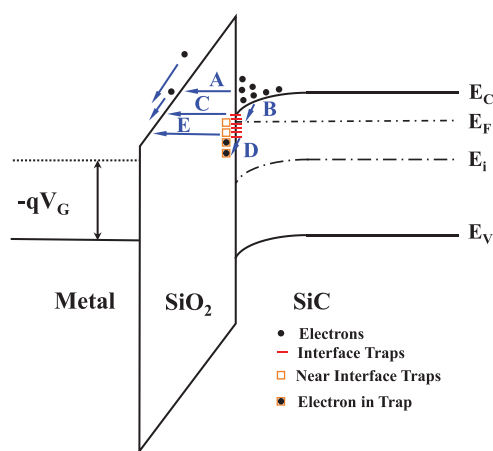


FIG. 5. Illustrates the conductive mechanisms of electrons labeled A–E. A: FN tunneling; B: electron trapping by interfacial charges; C: defect-assisted FN tunneling at the interface; D: electron detachment from interfacial defects followed by capture by near-interfacial oxide traps; E: near-interfacial defect-assisted FN tunneling.

This study investigates the impact of nitrogen passivation on the energy-level-dependent capture cross section distribution of SiO₂/SiC interface defects by local band bending modulation in temperature-variable DLTS characterizations. Combining capture cross section and the D_{it} distributions, as well as the charge generation in the dielectric layer, the mechanisms governing the temperature-dependence of leakage behavior for SiC MOS devices are elucidated. Contrary to expectations, while nitrogen passivation significantly reduces D_{it} , it concurrently amplifies the capture cross sections of interface defects across distinct energy levels, which is unreported in the literature. Simultaneously, an anomalous temperature-dependent leakage behavior, characterized by an initial decrease followed by an increase with rising temperature, is observed in both nitrogen-passivated and conventional thermally oxidized samples. This leakage behavior is attributed to electron trapping/detrapping dynamics at interfacial/near-interfacial defects. An interfacial defect-assisted FN tunneling mechanism is proposed, and it is suggested that the temperature dependence of leakage currents originates from the synergistic interplay between the energy-level-dependent capture cross section and D_{it} distribution. At shallow energy levels, high D_{it} dominates despite smaller capture cross sections, whereas deeper levels exhibit larger capture cross sections but lower D_{it} . Consequently, D_{it} governs leakage at low temperatures, while capture cross sections dominate at elevated temperatures, resulting in the observed non-monotonic leakage characteristics. The SiC MOS capacitor serves as a fundamental substructure and simplified model of SiC MOSFETs, and therefore, these findings about the SiC/SiO₂ interface properties and leakage current characteristics of MOS capacitors are applicable to SiC MOSFETs. Hence, this work provides critical insights for optimizing leakage characteristics and reliability in SiC MOSFET devices, offering a foundational framework for designing high-temperature, high-power electronic systems.

This work was supported by the Science Challenge Project.

AUTHOR DECLARATIONS

Conflict of Interest

The authors have no conflicts to disclose.

Author Contributions

Wende Huang: Conceptualization (equal); Data curation (equal); Formal analysis (equal); Investigation (equal); Methodology (equal); Project administration (equal); Supervision (equal); Validation (equal); Visualization (equal); Writing – original draft (equal); Writing – review & editing (equal). **Peng Dong:** Data curation (equal); Funding acquisition (equal); Investigation (equal); Methodology (equal); Validation (equal); Visualization (equal). **Nuoya Yang:** Formal analysis (equal); Investigation (equal); Methodology (supporting); Writing – review & editing (supporting). **Yao Ma:** Formal analysis (equal); Funding acquisition (lead); Investigation (equal); Validation (equal); Visualization (equal); Writing – review & editing (supporting). **Qian Xu:** Formal analysis (equal); Methodology (supporting). **ChengWen Fu:** Investigation (equal); Methodology (supporting). **Mingmin Huang:** Data curation (supporting); Funding acquisition (supporting); Supervision (equal). **Yun Li:** Data curation (supporting); Funding acquisition (supporting); Project administration (supporting); Resources (equal); Supervision (equal). **Zhimei Yang:** Data curation (supporting); Funding acquisition (supporting); Project administration (supporting); Resources (equal); Supervision (equal). **Min Gong:**

Resources (equal); Supervision (equal). **Dongguo He:** Funding acquisition (supporting); Methodology (supporting). **Qiuming He:** Funding acquisition (supporting); Methodology (supporting).

DATA AVAILABILITY

The data that support the findings of this study are available from the corresponding authors upon reasonable request.

REFERENCES

- ¹T. Kimoto, "Material science and device physics in SiC technology for high-voltage power devices," *Jpn. J. Appl. Phys., Part 1* **54**(4), 040103 (2015).
- ²M. Ruff, H. Mitlehner, and R. Helbig, *IEEE Trans. Electron Devices* **41**, 1040–1054 (1994).
- ³M. Cabello, V. Soler, G. Rius, J. Montserrat, J. Rebollo, and P. Godignon, *Mater. Sci. Semicond. Process.* **78**, 22–31 (2018).
- ⁴J. A. Cooper, M. R. Melloch, R. Singh, A. Agarwal, and J. W. Palmour, *IEEE Trans. Electron Devices* **49**, 658–664 (2002).
- ⁵P. Pande, S. Dimitrijević, D. Haasman, H. A. Moghadam, P. Tanner, and J. Han, *IEEE J. Electron Devices Soc.* **6**, 468–474 (2018).
- ⁶L.-F. Mao, *Appl. Surf. Sci.* **254**, 6628–6632 (2008).
- ⁷D. Zhai, D. Gao, J. Xiao, X. Gong, J. Yang, Y. Zhao, J. Wang, and J. Lu, *J. Phys. D: Appl. Phys.* **53**, 445102 (2020).
- ⁸R. Schomer, P. Friedrichs, D. Peters, and D. Stephani, *IEEE Electron Device Lett.* **20**, 241–244 (1999).
- ⁹V. V. Afanasev, M. Bassler, G. Pensl, and M. Schulz, "Intrinsic SiC/SiO₂ interface states," *Phys. Status Solidi A* **162**, 321–337 (1997).
- ¹⁰P. Deak, J. M. Knaup, T. Hornos, C. Thill, A. Gali, and T. Frauenheim, *J. Phys. D: Appl. Phys.* **40**, 6242–6253 (2007).
- ¹¹F. Devynck, A. Alkauskas, P. Broqvist, and A. Pasquarello, *Phys. Rev. B* **84**, 235320 (2011).
- ¹²A. V. Kimmel, P. V. Sushko, A. L. Shluger, and G. Bersuker, *ECS Trans.* **19**, 3–17 (2009).
- ¹³Y. Zhang, H. Li, Q. Wang, T. Chen, and L. Zhao, *IEEE Trans. Electron Devices* **71**, 7682–7688 (2024).
- ¹⁴G. Liu, Y. Wang, K. Sheng, B. Zhang, and F. Udreă, *IEEE Electron Device Lett.* **34**, 181–183 (2013).
- ¹⁵P. Fiorenza, L. K. Swanson, M. Vivona, A. Bassi, G. Greco, and F. Roccaforte, *Appl. Phys.* **115**, 33–339 (2014).
- ¹⁶Y. Iwasaki, H. Yano, T. Hatayama, Y. Uraoka, and T. Fuyuki, *Appl. Phys.* **3**, 026201 (2010).
- ¹⁷K. Tachiki, M. Kaneko, T. Kobayashi, and T. Kimoto, *Appl. Phys. Express* **13**, 121002 (2020).
- ¹⁸K. Tachiki and T. Kimoto, *IEEE Trans. Electron Devices* **68**, 638–644 (2021).
- ¹⁹D. Okamoto, H. Yano, K. Hirata, T. Hatayama, and T. Fuyuki, *IEEE Electron Device Lett.* **31**, 710–712 (2010).
- ²⁰J. Berens, G. Pobegen, G. Rescher, T. Aichinger, and T. Grasser, *IEEE Trans. Electron Devices* **66**, 4692–4697 (2019).
- ²¹G. Y. Chung, C. C. Tin, J. R. Williams, K. McDonald, R. K. Chanana, R. A. Weller, S. T. Pantelides, L. C. Feldman, O. W. Holland, M. K. Das, and J. W. Palmour, *IEEE Electron Device Lett.* **22**, 176–178 (2001).
- ²²C.-Y. Lu, J. A. Cooper, T. Tsuji, G. Chung, J. R. Williams, K. McDonald, and L. C. Feldman, *IEEE Trans. Electron Devices* **50**, 1582–1588 (2003).
- ²³M. Gurfinkel, J. Suehle, M. H. White, and Y. Flitsiyan, *IEEE Trans. Electron Devices* **55**, 2004–2012 (2008).
- ²⁴A. Chanthaphan, T. Hosoi, Y. Nakano, T. Nakamura, T. Shimura, and H. Watanabe, *Appl. Phys. Lett.* **102**, 093510 (2013).
- ²⁵A. J. Leis, D. B. Habersat, R. Green, and N. Goldsman, *Mater. Sci. Forum* **717–720**, 465–468 (2012).
- ²⁶P. Fiorenza, M. Vivona, F. Iucolano, A. Severino, S. Lorenti, G. Nicotra, C. Bongiorno, F. Giannazzo, and F. Roccaforte, *Mater. Sci. Semicond. Process.* **78**, 38–42 (2018).
- ²⁷I. S. Jeon, J. Park, D. Eom, C. S. Hwang, H. J. Kim, C. J. Park, H. Y. Cho, J.-H. Lee, N.-I. Lee, and H.-K. Kang, *Appl. Phys. Lett.* **82**, 1066–1068 (2003).
- ²⁸S. Ozder, I. Atılgan, and B. Katircioglu, *Semicond. Sci. Technol.* **10**, 1510–1519 (1995).
- ²⁹C. Gong, E. Simoen, N. E. Posthuma, E. V. Kerschaver, J. Poortmans, and R. Mertens, *J. Phys. D: Appl. Phys.* **43**, 485301 (2010).
- ³⁰P. Zhao, Rusli, Y. Liu, C. C. Tin, W. G. Zhu, and J. Ahn, *Microelectron. Eng.* **83**, 61–64 (2006).
- ³¹H. Yoshioka, T. Nakamura, and T. Kimoto, *J. Appl. Phys.* **115**, 014502 (2014).
- ³²H. Yoshioka, T. Nakamura, and T. Kimoto, *J. Appl. Phys.* **112**, 024520 (2012).
- ³³X. D. Chen, S. Dhar, T. Isaacs-Smith, J. R. Williams, L. C. Feldman, and P. M. Mooney, *J. Appl. Phys.* **103**, 033701 (2008).
- ³⁴E. Bano, T. Ouisse, L. Di Cioccio, and S. Karmann, *Appl. Phys. Lett.* **65**, 2723–2724 (1994).
- ³⁵Z. Wang, Z. Zhang, C. Shao, J. Robertson, S. Liu, and Y. Guo, *IEEE Trans. Electron Devices* **68**, 288–293 (2021).
- ³⁶Z. Qiaozhi, Q. Fuwen, L. Wenbo, and W. Dejun, *Appl. Phys. Lett.* **103**, 062105 (2013).
- ³⁷B. Liu, F. Qin, and D. Wang, *Appl. Surf. Sci.* **364**, 769–774 (2016).
- ³⁸P. Moens, J. Franchi, J. Lettens, L. D. Schepper, M. Domeij, and F. Allerstam, *Proc. IEEE* **78**–81 (2020).
- ³⁹S. R. Kodigala, *Physica B* **500**, 3543 (2016).
- ⁴⁰J. Berens, G. Pobegen, and T. Grasser, *Mater. Sci. Forum* **1004**, 652–658 (2020).
- ⁴¹T. Kobayashi, A. Suzuki, T. Nakanuma, M. Sometani, M. Okamoto, A. Yoshigoe, T. Shimura, and H. Watanabe, *Mater. Sci. Semicond. Process.* **175**, 108251 (2024).
- ⁴²E. D. Indari, Y. Yamashita, R. Hasunuma, T. Nagata, S. Ueda, and K. Yamabe, *AIP Adv.* **9**, 045002 (2019).
- ⁴³W. Tan, L. Zhao, C. Lu, W. Nie, and X. Gu, *Microelectron. Reliab.* **142**, 114907 (2023).
- ⁴⁴A. Xiang, X. Xu, L. Zhang, Z. Li, J. Li, and G. Dai, *Appl. Phys. Lett.* **112**, 062101 (2018).
- ⁴⁵Z. Ouenoughi, C. Strenger, F. Bourouba, V. Haeublein, H. Ryssel, and L. Frey, *Microelectron. Reliab.* **53**, 1841–1847 (2013).
- ⁴⁶T.-H. Kil, A. Tamura, S. Shimizu, and K. Kita, *Appl. Phys. Express* **14**, 081005 (2021).
- ⁴⁷K. Y. Cheong, J. H. Moon, H. J. Kim, W. Bahng, and N.-K. Kim, *J. Appl. Phys.* **103**, 084113 (2008).
- ⁴⁸M. Sometani, D. Okamoto, S. Harada, H. Ishimori, S. Takasu, T. Hatakeyama, M. Takei, Y. Yonezawa, K. Fukuda, and H. Okumura, *J. Appl. Phys.* **117**, 024505 (2015).